SCIENCE CHINA
Information Sciences

• RESEARCH PAPER •

December 2024, Vol. 67, Iss. 12, 222401:1–222401:10
https://doi.org/10.1007/s11432-023-3966-8

# Ultra-low power IGZO optoelectronic synaptic transistors for neuromorphic computing

Li ZHU[1*], Sixian LI[1], Junchen LIN[1], Yuanfeng ZHAO[1], Xiang WAN[1], Huabin SUN[1], Shancheng YAN[1], Yong XU[1], Zhihao YU[1], Chee Leong TAN[1*] & Gang HE[2*]

[1]*College of Integrated Circuit Science and Engineering, Nanjing University of Posts and Telecommunications, Nanjing* 210023*, China;*
[2]*School of Materials Science and Engineering, Anhui University, Hefei* 230601*, China*

Received 22 November 2023/Revised 6 January 2024/Accepted 27 February 2024/Published online 10 September 2024

**Abstract** Inspired by biological visual systems, optoelectronic synapses with image perception, memory retention, and preprocessing capabilities offer a promising pathway for developing high-performance artificial perceptual vision computing systems. Among these, oxide-based optoelectronic synaptic transistors are well-known for their enduring photoconductive properties and ease of integration, which hold substantial potential in this regard. In this study, we utilized indium gallium zinc oxide as a semiconductor layer and high-k $ZrAlO_x$ as a gate dielectric layer to engineer low-power high-performance synaptic transistors with photonic memory. Crucial biological synaptic functions, including excitatory postsynaptic currents, paired-pulse facilitation, and the transition from short-term to long-term plasticity, were replicated via optical pulse modulation. This simulation was sustained even at an operating voltage as low as 0.0001 V, exhibiting a conspicuous photonic synaptic response with energy consumption as low as 0.0845 fJ per synaptic event. Furthermore, an optoelectronic synaptic device was employed to model "learn-forget-relearn" behavior similar to that exhibited by the human brain, as well as Morse code encoding. Finally, a $3 \times 3$ device array was constructed to demonstrate its advantages in image recognition and storage. This study provides an effective strategy for developing readily integrable, ultralow-power optoelectronic synapses with substantial potential in the domains of morphological visual systems, biomimetic robotics, and artificial intelligence.

**Keywords** IGZO optoelectronic synaptic devices, persistent photoconductivity, ultra-low power, neuromorphic computing

## 1 Introduction

With the advent of artificial intelligence, traditional von Neumann-architecture-based computing systems have reached a bottleneck [1–4]. Unlike the serial computing approach of the von Neumann architecture, the human brain and sensory organs acquire, process, and transmit information in a parallel fashion [5–7]. This parallel information processing approach endows the human brain with exceptionally high efficiency and remarkably low power consumption [8]. The human brain comprises approximately $10^{11}$ neurons, with approximately $10^{15}$ synapses connecting them, forming a complex neural network that plays a crucial role in sensory perception, learning, and memory during neural activities [9–11]. Inspired by human perceptual computing systems, various types of neuromorphic devices have been used to simulate synapses and neurons [12–15]. Among these, optoelectronic synaptic devices are gaining increasing attention because of their advantages, such as light sensitivity, low power consumption, wide bandwidth, and minimal crosstalk [16, 17]. Hence, the construction of low-power, high-efficiency, and light-sensitive synaptic devices through structural design and material selection will contribute to the advancement of artificial neural morphological visual systems. Amorphous indium gallium zinc oxide (IGZO) thin-film transistors (TFTs) are highly valuable in the field of large-area displays and emerging storage industries due to their exceptional electrical and physical properties, including high carrier mobility ($> 10$ cm$^2$/(V $\cdot$ s)), large-area uniformity, low-temperature processing capabilities, and high transparency. As an n-type oxide

* Corresponding author (email: zhuli0319@njupt.edu.cn, cheelong@gmail.com, hegang@ahu.edu.cn)

 

semiconductor, the doping mechanism in IGZO involves oxygen vacancies (Vo), which generate two free electrons in the conduction band as shallow donors. The electron concentration increases as the Vo content of the IGZO film increases. The presence of a substantial number of oxygen vacancies leads to the characteristic persistent photoconductivity (PPC) of IGZO. Typically, the behavior of PPC can be explained by variations in the ionization and recombination of oxygen vacancies. When the IGZO channel is exposed to near-ultraviolet (NUV) light, deep-level localized oxygen vacancy (Vo) ionization into a shallow donor state ($Vo^+$ and $Vo^{2+}$) results in an increase in the channel conductivity owing to the generated electrons. Following the optical pulse, the electrons in IGZO slowly recombine with shallow donor states ($Vo^+$ and $Vo^{2+}$), leading to a gradual reduction in channel conductivity. The increase and decrease in the IGZO channel conductivity mirror the changes in the postsynaptic membrane potential induced by the entry and extrusion of $Ca^{2+}$ in the dynamic behavior of biological synapses. Consequently, IGZO transistors are particularly well-suited for emulating optoelectronic synaptic functions.

In addition, to attain a high channel current at a low operating voltage, high-k gate materials such as $HfO_2$ [18], $ZrO_2$ [19], and $TiO_2$ [20] can be utilized as gate dielectric layers. Among these exceptional gate dielectrics, $ZrO_2$ is regarded as one of the most promising because of its high dielectric constant ($\sim$25), wide bandgap (5.68 eV), and high transparency under visible light [21–23]. Nevertheless, $ZrO_2$ gate dielectrics often require cation doping to address issues such as high oxygen vacancy content and susceptibility to crystallization, which results in an increased leakage current and reduced breakdown field [24]. In contrast, $Al_2O_3$ with its high breakdown-field strength and amorphous structure, serves as an excellent complementary material for $ZrO_x$ [25]. Consequently, $ZrAlO_x$ gate dielectric layers have been prepared using atomic layer deposition (ALD) as ideal gate dielectrics for optoelectronic synaptic devices, facilitating the construction of low-power, high-performance optoelectronic synaptic transistors. Notably, both magnetron-sputtered IGZO and ALD-fabricated high-k materials are well-suited for contemporary integration processes.

In this study, low-power high-performance artificial optoelectronic synaptic transistors were constructed using IGZO channels and $ZrAlO_x$ gate dielectrics. By modulating optical pulses, the devices successfully emulated various biological synaptic functions, including excitatory postsynaptic currents (EPSCs), paired-pulse facilitation (PPF), the transition from short-term plasticity (STP) to long-term plasticity (LTP), and further mimicked the "learn-forget-relearn" behavior and Morse code encoding exhibited by the human brain using the optoelectronic synaptic device. Finally, a $3 \times 3$ device array was constructed to demonstrate the image recognition and storage capabilities of the proposed method. Notably, even at a $V_d$ as low as 0.0001 V, a distinct photonic synaptic response was achieved, with a power consumption of 0.0845 fJ per synaptic event. Our results indicate the potential for the large-scale integration of this optoelectronic synaptic device, contributing to the development of ultralow-power neural morphological perceptual computing systems.

## 2 Materials and methods

Artificial optoelectronic synaptic transistor devices were constructed using an Al/IGZO/$ZrAlO_x$/$P^{++}$Si structure. A highly boron-doped silicon substrate (resistivity of 0.002–0.004 $\Omega \cdot$ cm) was employed as the substrate. Before device fabrication, the substrates were meticulously cleaned by subjecting them to three cycles of ultrasonic cleaning in anhydrous ethanol and deionized water followed by drying with $N_2$ gas. Subsequently, at a temperature of 150°C, an ALD process was employed to alternately deposit $ZrO_x$ and $Al_2O_3$ films on the substrate, ultimately forming a 20 nm-thick $ZrAlO_x$ gate dielectric layer. Then, at room temperature, a 30 nm thick IGZO film (In:Ga:Zn = 2:2:1 atomic ratio) was radio-frequency sputtered under conditions of 0.3 Pa and 100 W. This was followed by annealing at 300°C for 1 h in a tube furnace. Finally, 100 nm of aluminum was thermally evaporated as the source-drain electrodes, with a channel width of 1000 μm and a length of 80 μm. Ultraviolet-visible (UV-Vis) spectroscopy (UV-2550) was used to characterize the absorption spectrum of IGZO, and atomic force microscopy (AFM, Asylum Cipher) was employed to analyze the surface morphologies of both the IGZO and $ZrAlO_x$ films. The electrical properties and synaptic characteristics were measured at room temperature with a relative humidity of approximately 50% using a semiconductor parameter analyzer (B1500) and a fiber-coupled laser module (PGL-FC-405).

## 3 Results and discussion

Figure 1(a) shows a schematic of the fabricated bottom-gate, top-contact TFT device. The IGZO functions as an n-type semiconductor layer, with the gate electrode receiving a positive gate voltage. This causes the accumulation of free electrons at the interface between the semiconductor and gate dielectric layer, forming a conductive channel, thereby generating a source-drain current. Because the formation of the conducting channel occurs at the interface between the semiconductor and insulating layers, the film quality at the interface affects the carrier transport to some extent. We investigated the surface roughness of IGZO and $ZrAlO_x$ films using AFM. As shown in Figure 1(b), the root-mean-square (RMS) surface roughness of the IGZO film is approximately 203 pm, whereas that of the $ZrAlO_x$ film is approximately 226 pm. The AFM test results indicated that the smooth surface morphology promoted the reduction of interface defects and leakage current resulting from surface roughness. Ultimately, this facilitates the construction of high-performance thin-film transistors with high mobility and very low subthreshold swing (SS) [26]. Subsequently, an IGZO film was deposited on the quartz glass for UV-vis spectroscopy. Figure 1(c) shows the absorption spectrum of the IGZO film. Furthermore, an $Al/ZrAlO_x/P^{++}Si$ structure was fabricated to investigate the dielectric properties of the gate dielectric films. Figure 1(d) shows the variation in the area capacitance of the $ZrAlO_x$ gate dielectric with frequency. The area capacitance is approximately 160 $nF/cm^2$ at 1 Hz.

Subsequently, the electrical characteristics of the transistor were tested at room temperature. Figures 1(e) and (f) respectively illustrate the output and transfer characteristics of the optoelectronic synaptic transistor. Figure 1(e) shows the typical output characteristics of an n-type transistor. As the gate voltage ($V_g$) increased from 0 to 2 V, the source-drain current ($I_d$) also increased. At $V_d = 2.5$ V and $V_g = 2.0$ V, the output curve exhibits a well-defined pinch-off voltage and a saturation current of 79 μA. Figure 1(f) shows the transfer characteristics of the device. As the gate voltage sweeps from −2 to 3 V, the $I_d$-$V_g$ curve exhibits minimal clockwise hysteresis, indicating effective treatment of interface traps in the conducting channel and maintaining low leakage current levels ($I_g = 10^{-11}$ A). Furthermore, the device was turned on near 0 V, indicating an enhancement-mode n-type transistor device with excellent transfer characteristics. To further assess the device's electrical performance, subthreshold swing (SS) and saturation mobility ($\mu$) can be calculated using the following equations:

$$\mathrm{SS} = \left(\frac{\mathrm{d}\log\left(I_{\mathrm{DS}}\right)}{\mathrm{d}V_{\mathrm{GS}}}\right)^{-1}, \tag{1}$$

$$I_{\mathrm{DS}} = \left(\frac{W}{2L}C_i\mu\right)\left(V_{\mathrm{GS}} - V_{\mathrm{TH}}\right)^2. \tag{2}$$

In (2), $C_i$ represents the area capacitance of the $ZrAlO_x$ gate dielectric. The calculations yield SS and saturation mobility values of 69 mV/dec and 25.5 cm/(V · s), respectively. The device exhibited excellent electrical characteristics with a high $I_{on}/I_{off}$ of $1.9 \times 10^8$. These findings establish a strong foundation for subsequent studies on light-stimulated synaptic behavior.

Further investigations focused on the photoelectric transport characteristics of the transistor. Figure 2(a) shows a schematic of the structure of an optoelectronic synaptic device based on IGZO. The response of the device to optical pulses can be explained by changes in oxygen vacancy ionization and recombination within the IGZO semiconductor layer, as shown in Figure 2(b). The oxygen vacancies in the IGZO channel exist in three states: shallow donor states ($Vo^+$ and $Vo^{2+}$) and deep localized states (Vo). When exposed to optical pulse stimulation, Vo undergoes ionization, inducing the release of free electrons ($Vo \rightarrow Vo^+ + e^-$ or $Vo \rightarrow Vo^{2+} + 2e^-$), leading to an increase in IGZO channel conductivity and resulting in the typical EPSC phenomenon. After the optical pulse is removed, the electrons in IGZO continue to recombine ($Vo^+ + e^- \rightarrow Vo$ and $Vo^{2+} + 2e^- \rightarrow Vo$), causing a gradual reduction in channel conductivity. Figure 2(c) shows the characteristic transfer curves of the device under pulsed illumination at different optical power densities. $V_d$ is fixed at 3 V, and $V_g$ is scanned from −2 to 3 V. The threshold voltage ($V_{TH}$) shifted to the left (towards a negative gate bias) with increasing light power density, indicating that a higher density of photogenerated carriers accelerated the formation of the conducting channel. With a further increase in the light power density, the growth of the photocurrent gradually approaches saturation, which is attributed to the saturation of light absorption in the IGZO semiconductor layer and defect states in the $ZrAlO_x$ dielectric layer at higher light power densities. To quantitatively

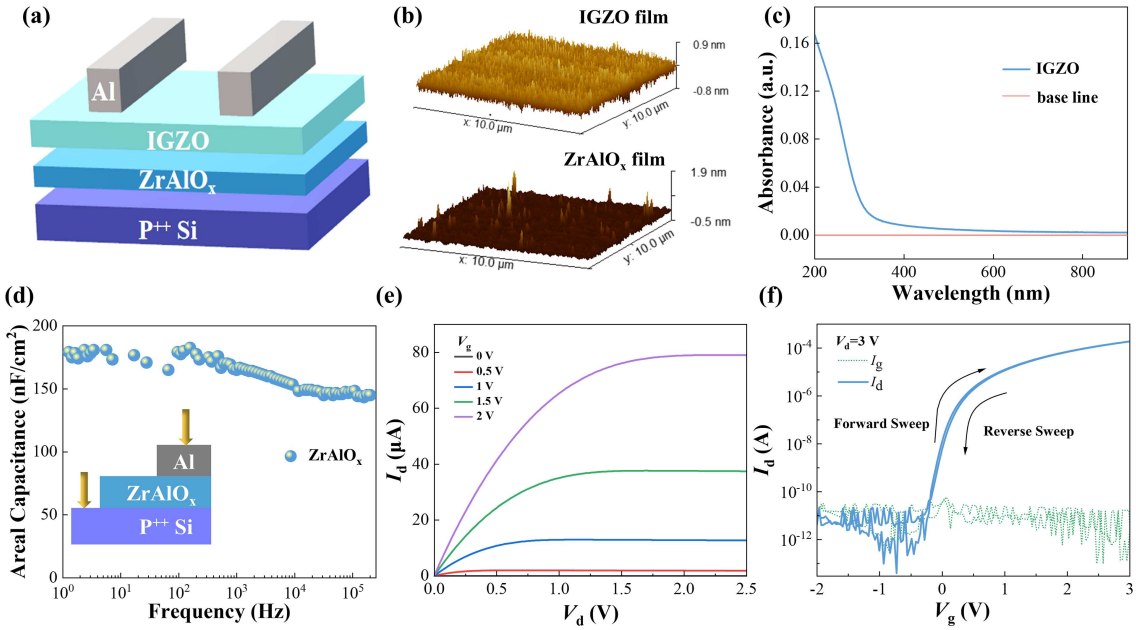


**Figure 1** (Color online) Device schematic and characterization. (a) Device structure schematic; (b) schematics of IGZO and $ZrAlO_x$ AFM images; (c) ultraviolet-visible absorption spectrum of the IGZO film; (d) variation in the capacitance of $ZrAlO_x$ dielectric with frequency; (e) output characteristics curve of the IGZO transistor; (f) transfer characteristics curve of the IGZO optoelectronic synaptic transistor.

assess the light response of the device, the following equations were used to calculate the responsivity ($R$), specific detectivity ($D^*$), and external quantum efficiency (EQE) of the device:

$$R = J_{\rm ph}/L_{\rm light}, \tag{3}$$

$$D^* = \sqrt{A} \times R/\sqrt{2q \times I_{\rm dark}}, \tag{4}$$

$$\text{EQE} = R \times \text{hc}/q\lambda. \tag{5}$$

In (3)–(5), $J_{\rm ph}$ represents the photocurrent density, $L_{\rm light}$ is the incident light power density, h denotes the Planck constant, c represents the speed of light, $q$ represents the elementary charge, and $I_{\rm dark}$ corresponds to the dark current. As shown in Figures 2(d) and (e), at an optical power density of 0.39 mW/cm$^2$ ($V_{\rm d}$ = 3 V), $R$, EQE, and $D^*$ reach values of 40.7 A · W$^{-1}$, 124.78%, and 1.547 × 10$^{15}$ Jones (1 Jones = 1 cm × HZ$^{1/2}$ · W$^{-1}$), respectively. This indicated that the device was highly sensitive to light.

Figure 3(a) shows the schematic relationship between the human visual system and neural synapses. The retina receives optical information from the environment and transmits it to the visual cortex of the human brain, which is then relayed through synaptic structures between neurons [27]. Biological synapses are fundamental units for information transmission and regulation in the human brain and serve as sites where synaptic neurons are functionally interconnected. Typically, neurotransmitters released by presynaptic neurons in response to external stimuli bind to receptors on the postsynaptic membrane, generating EPSC in postsynaptic neurons. This process strongly resembles the motion of photogenerated carriers, enabling artificial optoelectronic synaptic devices to simulate the critical functions of biological synapses. Using 405 nm light pulses as presynaptic stimuli and the device as the postsynaptic membrane, free electrons in the conducting channel act as neurotransmitters. Compared to electrical signals, light signals offer advantages such as high bandwidth, nondestructive operation, and high operation speed. Figure 3(b) shows the typical EPSC behavior induced by 405 nm light pulses (0.39 mW/cm$^2$, 0.3 s) under the conditions of $V_{\rm d}$ at 1 V and $V_{\rm g}$ at 0 V. When the light pulse stimulus is applied, the current increases from an initial 16.1 to 83.4 pA, and after removing the light pulse, the current gradually starts to decay. This behavior closely resembles that of a biological synapse.

PPF is a characteristic feature of STP that plays a vital role in the recognition and interpretation of visual, auditory, and other signals in the biological nervous system [28,29]. This phenomenon occurs when two consecutive stimuli of equal intensity are delivered, during which the EPSC induced by the second stimulus is stronger than the EPSC generated by the first stimulus [30]. As depicted in Figure 3(c), we

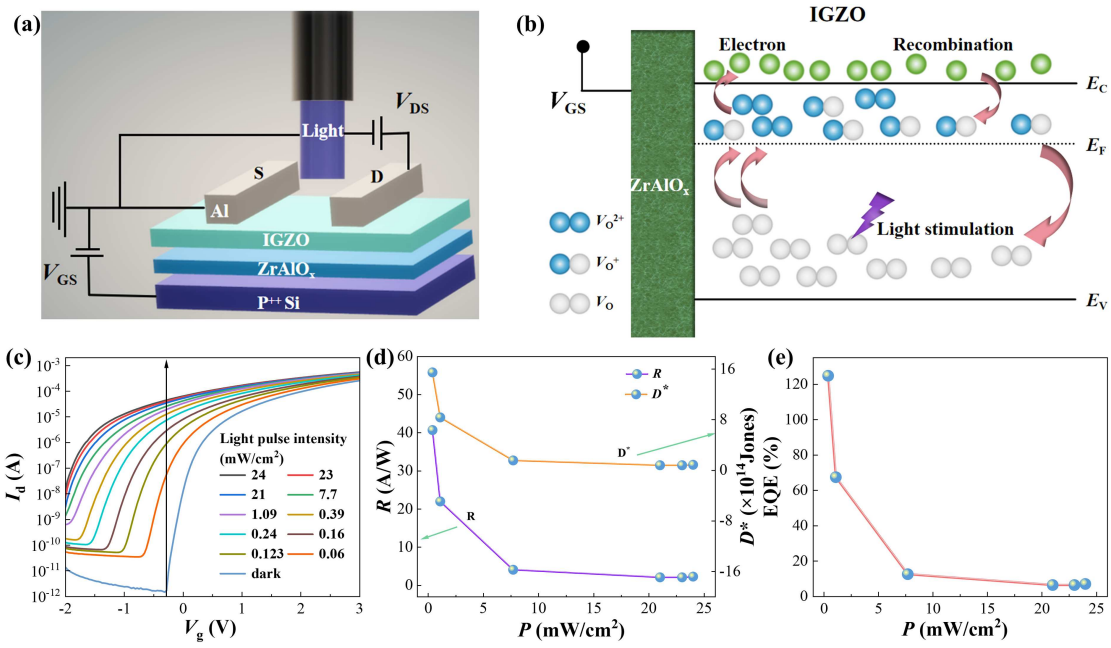


**Figure 2** (Color online) Photodetector light response. (a) Schematic illustrating light stimulation in the optoelectronic synaptic device based on IGZO; (b) mechanism diagram depicting the ionization and recombination process of oxygen vacancies in IGZO under light stimulation; (c) transfer characteristics curves at different light power densities; (d) relationship between responsivity and detectivity with light power density; (e) EQE and light power density graph.

administered two successive light pulses to the device (0.39 mW/cm$^2$, 405 nm, 0.3 s), with a 0.9 s interval between them. The results demonstrate a significantly greater EPSC for the second pulse than for the first pulse. This occurs because the photogenerated electrons from the initial light stimulation had not fully recombined when the subsequent light pulse was administered within a relatively short timeframe, and the photogenerated electrons from the first light stimulation had not fully recombined. When the light pulse was applied again for a relatively short time, the photogenerated electrons generated by the second pulse and those that had not yet recombined from the previous pulse accumulated, which resulted in a greater EPSC for the device during the second pulse and demonstrated typical PPF behavior. The calculation method for the PPF index is PPF $= A2/A1 \times 100\%$, where $A1$ and $A2$ represent the $\Delta$EPSC values achieved by the first and second light stimulations, respectively. Figure 3(d) shows the relationship between the pulse interval (0.3–6 s) and the PPF index. As the interval time increased, the PPF exhibited exponential decay. This was because when the interval between two consecutive light pulses increased further, most of the photogenerated electrons recombined before the second light pulse arrived, which led to a decrease in the current. Therefore, the PPF index decreased with increasing intervals between light stimulations. This relationship is consistent with the patterns observed in biological synapses [31–33].

Memory can be categorized into short-term memory (STM) and long-term memory (LTM) based on the duration of information retention. The memory capacity of the human brain is related to the intensity of learning, and the transition from STP to LTP at biological synapses can be achieved through repeated learning and consolidation [34]. Using our device, synaptic plasticity can be controlled by changing the pulse width, number of pulses, and pulse intensity. As shown in Figure 4(a), when the pulse width increased from 200 ms to 4 s, the EPSC increased from 0.191 to 4.26 nA. This is because a longer exposure time resulted in an increased number of photogenerated charge carriers, leading to a sustained increase in the EPSC. Furthermore, after light stimulation ended, the synaptic devices exhibited more pronounced LTM behavior as the pulse width increased, maintaining a high memory current over an extended period, which aligns with the pattern of consolidating information in LTM in the human brain. In addition, similar control phenomena were observed with varying pulse numbers and pulse intensities in the photonic synapses, as shown in Figure 4(b). When 1, 2, 5, 8, 10, and 15 pulses were used to stimulate the device, the EPSC increased from 0.195 to 1.02 nA as the number of pulses increased from 1 to 15. Moreover, with an increasing number of pulses, there was a transition from STP to LTP after the light stimulation ended, following the human brain's process of retaining information through repetition. Figure 4(c) shows the effect of the pulse intensity on the current magnitude. As the pulse intensity

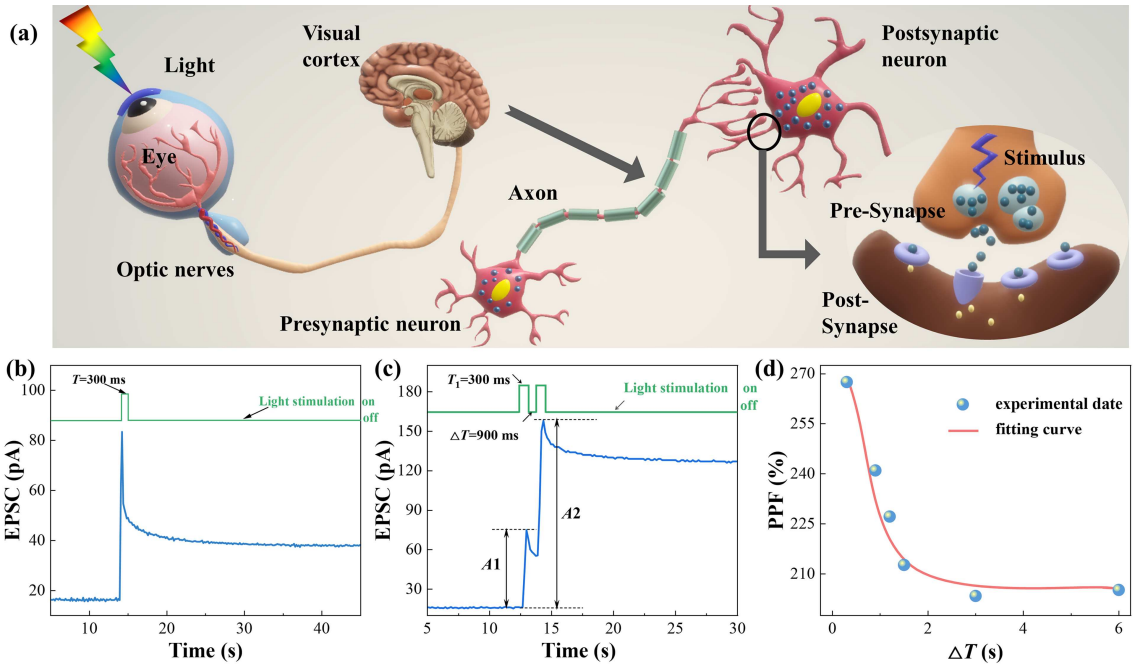


**Figure 3** (Color online) Synaptic plasticity in IGZO optoelectronic transistor. (a) Schematic relationship between the human visual system and neural synapses; (b) EPSC triggered by a single light pulse (0.39 mW/cm$^2$, 405 nm, 0.3 s), $V_d$ = 1 V; (c) EPSC triggered by two consecutive light pulses (0.39 mW/cm$^2$, 405 nm, 0.3 s) with an interval of 0.9 s, $V_d$ = 1 V; (d) relationship between the interval time ($\Delta T$) of two consecutive light pulses and the PPF index. The light intensity is fixed at 0.39 mW/cm$^2$, and the light pulse duration is 0.3 s.

increased from 0.16 to 24 mW/cm$^2$, the corresponding EPSC increased from 0.195 to 1.02 nA. This also reflects the characteristic transition from STP to LTP with increasing pulse intensity, which is consistent with the human brain pattern of memory deepening through strong stimulation. Figures 4(d)–(f) show the statistical data on the weight changes of these behaviors. The weight change value is defined as $\Delta W = (I_t - I_o/I_o)\times 100\%$, where $I_t$ is the current value of EPSC after the removal of light pulses, which decays naturally at 20 and 60 s, and $I_o$ is the initial current value. Statistical data indicated that the decay time increased with increasing pulse width, pulse number, and pulse intensity, demonstrating a successful transition from STP to LTP in the synapses, consistent with the principles of human memory.

The Ebbinghaus forgetting curve demonstrates that if an individual fails to engage in timely memory recall after learning, their memory gradually declines until complete forgetting occurs [35]. As shown in Figure 5(a), short-term and long-term potentiation of synapses serves as the foundation for learning and memory in the human brain. Consequently, we simulated the "learning-forgetting-relearning" behavior of the human brain by applying consecutive light pulses (405 nm, 0.3 s, 0.39 mW/cm$^2$) to the optoelectronic synaptic device in our study. As shown in Figure 5(b), 20 light pulses were initially used to stimulate the device for LTM behavior, followed by a forgetting period of 100 s. Subsequently, only six light pulses were required for repeated memory recall to achieve the previous memory level. Among these patterns, "•" represents light pulses with a duration of 0.2 s, whereas "-" represents light pulses with a duration of 1 s. Stimulation was performed using light pulses with a power density of 10 mW/cm$^2$. As observed in Figures 5(c) and (d), each Arabic numeral induced a distinct EPSC response, indicating that meaningful information can be conveyed through the EPSC response. This feature supports its potential for information transmission in the context of optical wireless communication in human-computer interfaces.

The visual system is one of the most important sensory systems in humans and is responsible for processing a major portion of the information received by the brain from the external world [36,37]. As shown in Figure 6(a), we constructed an array of nine devices to form a 3 × 3 artificial visual array. We applied light pulse stimulation to five of these devices, creating an array of the letter "L" and the size of the resulting EPSC corresponded to the set chromaticity. As shown in Figure 6(b), during the learning process, as the number of light pulses increased from 1 to 10, the EPSC values of the five devices increased from 0.292, 0.351, 0.253, 0.342, and 0.343 nA to 2.21, 2.32, 1.37, 2.31, and 2.62 nA. With a gradual increase in the EPSC, the corresponding chromaticity colors deepened. Subsequently, the forgetting process began, and as the forgetting time increased from 1 to 100 s, the EPSC values for the

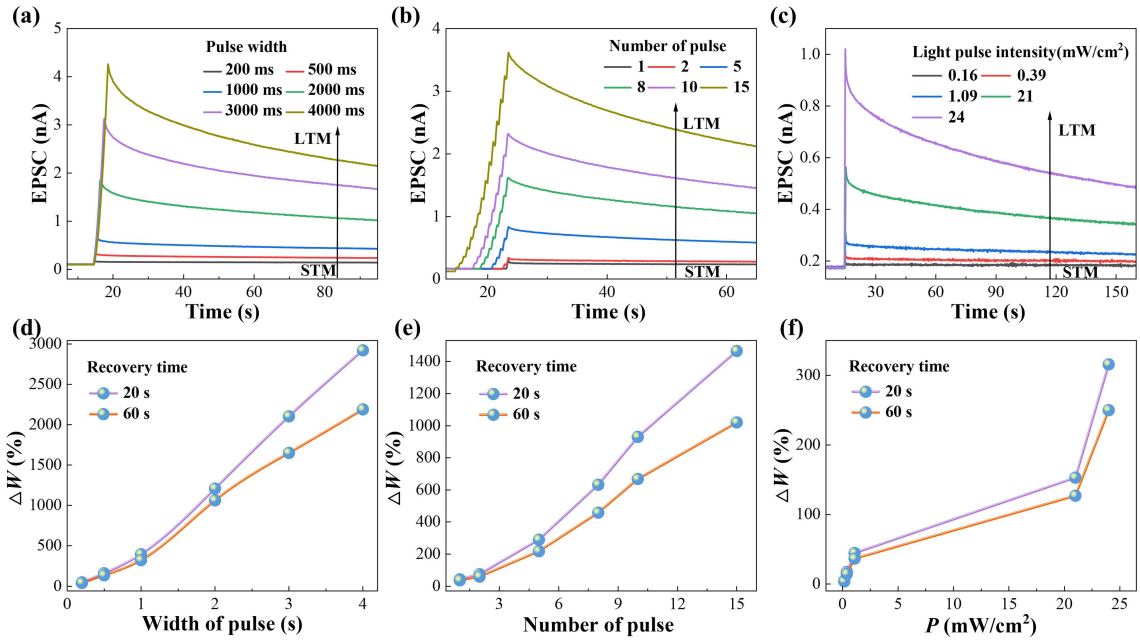


**Figure 4** (Color online) STP to LTP transition based on IGZO optoelectronic synaptic devices. (a) Variation in light pulse width (0.39 mW/cm$^2$, 405 nm); (b) effects of light pulse count (0.39 mW/cm$^2$, 405 nm, 0.3 s); (c) device response to changes in light intensity (405 nm, 0.3 s); (d)–(f) statistical analysis of weight change values 20 and 60 s after removing light pulses. Statistical categories correspond to different pulse widths, pulse counts, and light intensities.

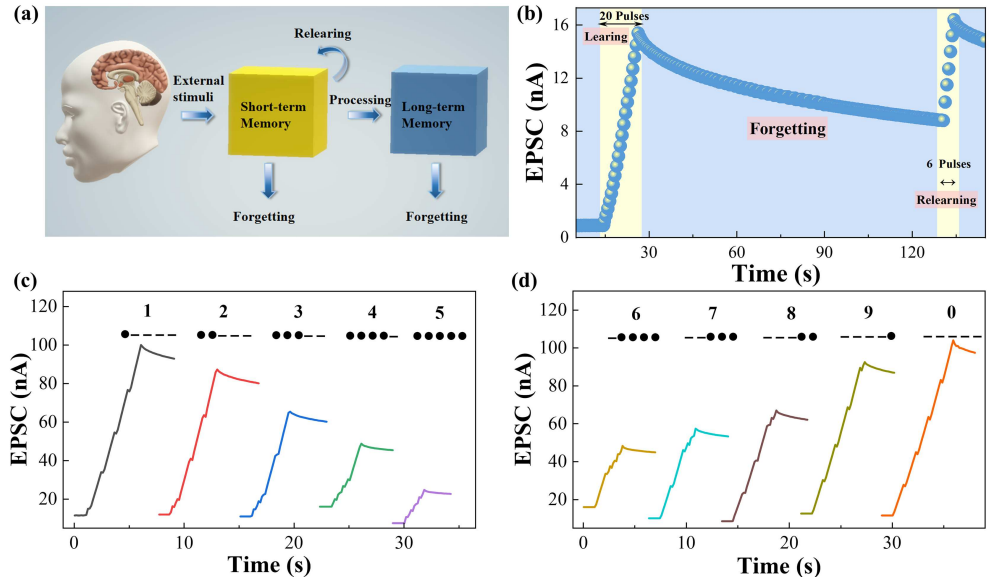


**Figure 5** (Color online) Learning-forgetting-relearning process and Morse code. (a) The law of human brain learning and forgetting; (b) learning, forgetting, and relearning process in a device resembling the human brain stimulated by pulsed light (0.39 mW/cm$^2$, 405 nm, 0.3 s); (c) and (d) induction of EPSC using a series of violet light pulses (405 nm, 0.39 mW/cm$^2$) and international Morse code representing Arabic numerals (0–9). The duration of dots and dashes in the pulses is 0.2 and 1 s, respectively, with a fixed interval of 0.2 s between two consecutive pulses.

devices that were stimulated with light pulses ten times decreased from 2.14, 2.21, 1.28, 2.22, 2.48 nA to 0.876, 0.971, 0.891, 1.01, 1.45 nA. As the EPSC decayed, the corresponding chromatic colors became lighter, demonstrating a dynamic forgetting process. Even after a 100-second interval, the array could still present a very clear image, and the color consistency of all five devices adhered to the principles of human memory and forgetting. This illustrates that our artificial visual array can store and retrieve information. Furthermore, this indicates that light-sensitive synaptic devices can simulate the learning and forgetting processes of the human brain, and the uniformity of the chromaticity highlights the stability of the

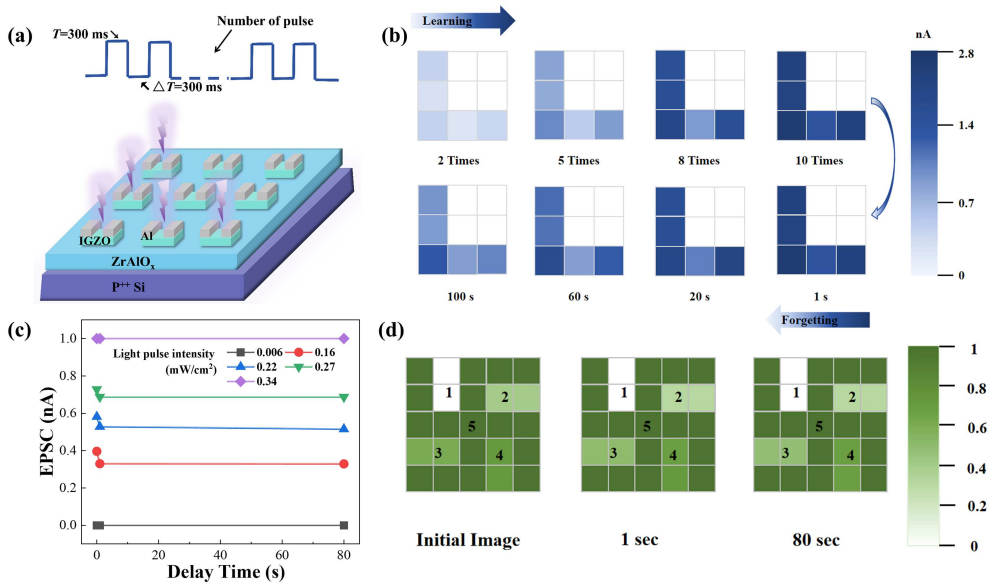


**Figure 6** (Color online) Dynamic learning and forgetting process, and image contrast enhancement demonstration of the photoelectric synapse array. (a) Schematic of the IGZO photoelectric synapse device array; (b) simulation of the learning and forgetting processes in the array. In the learning phase, different numbers of light pulses (2 times, 5 times, 8 times, 10 times) represent different learning frequencies. In the forgetting phase, the time after the light pulses were removed (1 s, 20 s, 60 s, 100 s) represents different stages of forgetting. $V_{\rm d}$ = 1 V, $V_{\rm g}$ = 0 V. (c) Changes in device current after removing light; (d) schematic of the array used for image contrast enhancement, with image contrast increasing over time.

device's performance [38]. Contrast enhancement is vital for improving image recognition accuracy.

Figure 6(c) depicts the changes in the normalized pixel output currents of the synaptic array under the influence of the light intensity. As shown in Figure 6(d), the light intensity had an important impact on contrast enhancement. The positions labeled 1, 2, 3, 4, and 5 in the image correspond to light intensities of 0.006, 0.16, 0.22, 0.27, and 0.34 mW/cm$^2$, respectively. All the current values were normalized. The initial values of these pixels were 0, 0.396, 0.581, 0.728, and 1. After removing the light pulse for 1 s, the values for these pixels were 0, 0.33, 0.528, 0.687, and 1. After 80 s, the values were 0, 0.329, 0.515, 0.687, and 1. It is noticeable that with a higher light intensity, the current decay is slower. For positions "2" and "3" corresponding to light intensities of 0.16 and 0.22 mW/cm$^2$, the normalized contrast decay was more pronounced compared to position "4" which corresponded to a light intensity of 0.27 mW/cm$^2$. Position "5" corresponded to the image of the character "swastika" and its contrast gradually increased as the decay time increased. Therefore, it is possible to use light intensity to enhance the contrast of images, indicating that this device has great potential for artificial image processing.

Low-energy-consumption photoelectric synaptic devices hold promise for achieving a high-efficiency artificial neural morphology platform, representing the developmental trend of photoelectric synaptic devices. In general, the energy consumption of each synaptic event can be expressed as follows: $E = V_{\rm d} \times I_{\rm d} \times t_{\rm spike}$ [39], where $V_{\rm d}$ represents the voltage applied between the source and drain, $I_{\rm d}$ represents the change in the EPSC after the light pulse stimulus, and $t_{\rm spike}$ is the pulse width. Therefore, $E$ is related to $V_{\rm d}$, $I_{\rm d}$, and the pulse width. To study the low-voltage operation characteristics of this photoelectric synapse device, we aimed to obtain a smaller EPSC triggered by light pulses by applying the smallest possible source-drain voltage and pulse width. As shown in Figure 7(a), to achieve low energy consumption, we used a short pulse width of 50 ms and a light pulse intensity of 0.06 mW/cm$^2$ to stimulate the device. We obtained significant EPSC behavior when $V_{\rm d}$ was set to 0.001 and 0.0001 V, for which the calculated power consumption values were 1.825 and 0.0845 fJ, respectively. Therefore, we achieved a minimum power consumption of 0.0845 fJ, which is significantly lower than the energy consumed by a single biological synapse (1–100 fJ) [40, 41]. Figure 7(b) shows the energy consumption of individual synaptic events in photoelectric synaptic transistors published in recent years [36, 42–50]. This device's energy consumption is better than most reported photoelectric synaptic devices, indicating its value in low-power, high-performance synaptic transistor applications and visual perception systems.

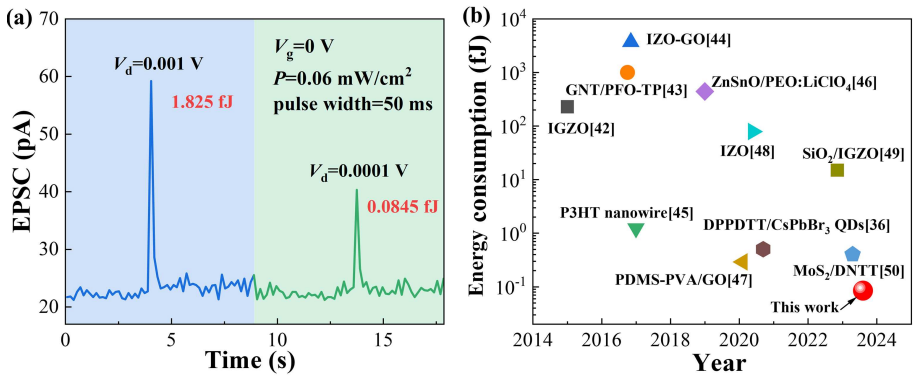


**Figure 7** (Color online) Low power. (a) EPSC triggered by light pulses with a pulse width of 50 ms at $V_d$ values of 0.001 and 0.0001 V, respectively; (b) a comparison of energy consumption between this photoelectric synaptic device and previously reported devices.

## 4 Conclusion

A low-power high-performance oxide photoelectric synaptic transistor based on an IGZO semiconductor and a $ZrAlO_x$ gate dielectric was constructed. It exhibited a saturation mobility of 25.5 cm/(V · s), a subthreshold swing (SS) of 69 mV/dec, and an $I_{on}/I_{off}$ of $1.9\times10^8$. Furthermore, excellent responsiveness to 405 nm light was detected. We successfully simulated various important biological synaptic functions using the persistent photoconductive behavior of oxide materials, including EPSC, PPF, STP-to-LTP transition, dynamic learning and forgetting behavior, and Morse code behavior. To further mimic the human visual neural network, a $3 \times 3$ artificial vision array was created that demonstrated color array recognition and enhanced image contrast at different light intensities. Even at $V_d = 0.0001$ V, the device still exhibited significant photo-synaptic responses, achieving a power consumption of 0.0845 fJ per individual synaptic event.

**Acknowledgements** This work was financially supported by National Natural Science Foundation of China (Grant Nos. 52105369, 61974070), Natural Science Foundation of the Jiangsu Higher Education Institutions of China (Grant No. 23KJB510014), and Natural Science Research Start-up Foundation of Recruiting Talents of Nanjing University of Posts and Telecommunications (Grant No. NY222061), Scientific Research Project of Colleges and Universities in Anhui Province (Grant No. 2022AH050113), and University Synergy Innovation Program of Anhui Province (Grant No. GXXT-2022-012).

**References**

1 Zidan M A, Strachan J P, Lu W D. The future of electronics based on memristive systems. Nat Electron, 2018, 1: 22–29
2 Wang Z R, Joshi S, Savel'ev S E, et al. Memristors with diffusive dynamics as synaptic emulators for neuromorphic computing. Nat Mater, 2017, 16: 101–108
3 Choi S, Tan S H, Li Z, et al. SiGe epitaxial memory for neuromorphic computing with reproducible high performance based on engineered dislocations. Nat Mater, 2018, 17: 335–340
4 Prezioso M, Merrikh-Bayat F, Hoskins B D, et al. Training and operation of an integrated neuromorphic network based on metal-oxide memristors. Nature, 2015, 521: 61–64
5 Kim Y, Chortos A, Xu W, et al. A bioinspired flexible organic artificial afferent nerve. Science, 2018, 360: 998–1003
6 Lee Y, Lee T W. Organic synapses for neuromorphic electronics: from brain-inspired computing to sensorimotor nervetronics. Acc Chem Res, 2019, 52: 964–974
7 Tan H, Tao Q, Pande I, et al. Tactile sensory coding and learning with bio-inspired optoelectronic spiking afferent nerves. Nat Commun, 2020, 11: 1369
8 He L H, Li E L, Yu R J, et al. Multistage photosynaptic transistor based on the regulation of ferroelectric P(VDF-TrFE) (in Chinese). Acta Photonica Sinic, 2021, 50: 0904002
9 Dai S, Zhao Y, Wang Y, et al. Recent advances in transistor-based artificial synapses. Adv Funct Mater, 2019, 29: 1903700
10 Hao D, Liu D, Zhang J, et al. Lead-free perovskites-based photonic synaptic devices with logic functions. Adv Mater Technologies, 2021, 6: 2100678
11 Wang H, Yang M, Tang Q, et al. Flexible, conformal organic synaptic transistors on elastomer for biomedical applications. Adv Funct Mater, 2019, 29: 1901107
12 Kuzum D, Jeyasingh R G D, Lee B, et al. Nanoelectronic programmable synapses based on phase change materials for brain-inspired computing. Nano Lett, 2012, 12: 2179–2186
13 Zhou J, Liu Y, Shi Y, et al. Solution-processed chitosan-gated IZO-based transistors for mimicking synaptic plasticity. IEEE Electron Device Lett, 2014, 35: 280–282
14 He Y, Nie S, Liu R, et al. Indium-gallium-zinc-oxide Schottky synaptic transistors for silent synapse conversion emulation. IEEE Electron Device Lett, 2019, 40: 139–142
15 Wang J, Li Y, Yin C, et al. Long-term depression mimicked in an IGZO-based synaptic transistor. IEEE Electron Device Lett, 2017, 38: 191–194
16 Li H K, Chen T P, Liu P, et al. A light-stimulated synaptic transistor with synaptic plasticity and memory functions based on InGaZnO$_x$-Al$_2$O$_3$ thin film structure. J Appl Phys, 2016, 119: 244505

17 Jang J T, Park J, Ahn B D, et al. Study on the photoresponse of amorphous In-Ga-Zn-O and zinc oxynitride semiconductor devices by the extraction of sub-gap-state distribution and device simulation. ACS Appl Mater Interfaces, 2015, 7: 15570–15577
18 Lee S Y, Chang S, Lee J S. Role of high-k gate insulators for oxide thin film transistors. Thin Solid Films, 2010, 518: 3030–3032
19 Ha T J, Dodabalapur A. Photo stability of solution-processed low-voltage high mobility zinc-tin-oxide/$ZrO_2$ thin-film transistors for transparent display applications. Appl Phys Lett, 2013, 102: 123506
20 Kumar A, Mondal S, Koteswara Rao K S R. Critical investigation of high performance spin-coated high-$\kappa$ titania thin films based MOS capacitor. J Mater Sci-Mater Electron, 2016, 27: 5264–5270
21 Yao R H, Zheng Z K, Xiong M, et al. Low-temperature fabrication of sputtered high-$k$ $HfO_2$ gate dielectric for flexible a-IGZO thin film transistors. Appl Phys Lett, 2018, 112: 103503
22 Shao Y, Xiao X, He X, et al. Low-voltage a-InGaZnO thin-film transistors with anodized thin $HfO_2$ gate dielectric. IEEE Electron Device Lett, 2015, 36: 573–575
23 Su N C, Wang S J, Chin A. High-performance InGaZnO thin-film transistors using HfLaO gate dielectric. IEEE Electron Device Lett, 2009, 30: 1317–1319
24 Zhu L, He G, Li W, et al. Nontoxic, eco-friendly fully water-induced ternary Zr-Gd-O dielectric for high-performance transistors and unipolar inverters. Adv Elect Mater, 2018, 4: 1800100
25 Yang W, Song K, Jung Y, et al. Solution-deposited Zr-doped $AlO_x$ gate dielectrics enabling high-performance flexible transparent thin film transistors. J Mater Chem C, 2013, 1: 4275–4282
26 Zhu L, He G, Zhang C, et al. Water-derived all-oxide thin-film transistors with $ZrAlO_x$ gate dielectrics and exploration in digital circuits. IEEE Trans Electron Devices, 2019, 66: 4198–4204
27 Fang Y Q, Li Q X, Meng J L, et al. Photonic synapses for image recognition and high density integration of simplified artificial neural networks. Adv Elect Mater, 2023, 9: 2300120
28 Han C, Han X W, Han J Y, et al. Light-stimulated synaptic transistor with high PPF feature for artificial visual perception system application. Adv Funct Mater, 2022, 32: 2113053
29 Xiong H, Xu L, Gao C, et al. Optically modulated $HfS_2$-based synapses for artificial vision systems. ACS Appl Mater Interfaces, 2021, 13: 50132–50140
30 Wei P, Wang X D, Li X L, et al. Reconfigurable multifunctional ambipolar polymer-blend transistors with improved switching-off capability. Adv Funct Mater, 2021, 31: 2103369
31 Zucker R S, Regehr W G. Short-term synaptic plasticity. Annu Rev Physiol, 2002, 64: 355–405
32 Dai S, Wu X, Liu D, et al. Light-stimulated synaptic devices utilizing interfacial effect of organic field-effect transistors. ACS Appl Mater Interfaces, 2018, 10: 21472–21480
33 Zhong Y N, Wang T, Gao X, et al. Synapse-like organic thin film memristors. Adv Funct Mater, 2018, 28: 1800854
34 Liu W Q, Wang H L, Liu F W, et al. Hybrid bacteriorhodopsin/zinc oxide synaptic photoconductors for bio-compatible neuromorphic devices. Adv Funct Mater, 2023, 33: 2302135
35 Zhang J Y, Liu D P, Shi Q Q, et al. Bioinspired organic optoelectronic synaptic transistors based on cellulose nanopaper and natural chlorophyll-a for neuromorphic systems. npj Flex Electron, 2022, 6: 30
36 Hao D, Zhang J, Dai S, et al. Perovskite/organic semiconductor-based photonic synaptic transistor for artificial visual system. ACS Appl Mater Interfaces, 2020, 12: 39487–39495
37 Islam M M, Krishnaprasad A, Dev D, et al. Multiwavelength optoelectronic synapse with 2D materials for mixed-color pattern recognition. ACS Nano, 2022, 16: 10188–10198
38 Yang B, Lu Y, Jiang D H, et al. Bioinspired multifunctional organic transistors based on natural chlorophyll/organic semiconductors. Adv Mater, 2020, 32: 2001227
39 Wang Y, Lv Z, Chen J, et al. Photonic synapses based on inorganic perovskite quantum dots for neuromorphic computing. Adv Mater, 2018, 30: 1802883
40 Wang C, Liu H, Chen L, et al. Ultralow-power synaptic transistor based on wafer-scale $MoS_2$ thin film for neuromorphic application. IEEE Electron Device Lett, 2021, 42: 1555–1558
41 Xu W T, Min S Y, Hwang H, et al. Organic core-sheath nanowire artificial synapses with femtojoule energy consumption. Sci Adv, 2016, 2: 2375–2548
42 Zhou J M, Liu N, Zhu L Q, et al. Energy-efficient artificial synapses based on flexible IGZO electric-double-layer transistors. IEEE Electron Device Lett, 2015, 36: 198–200
43 Feng P, Xu W W, Yang Y, et al. Printed neuromorphic devices based on printed carbon nanotube thin-film transistors. Adv Funct Mater, 2017, 27: 1604447
44 Yang Y, Wen J, Guo L Q, et al. Long-term synaptic plasticity emulated in modified graphene oxide electrolyte gated IZO-based thin-film transistors. ACS Appl Mater Interfaces, 2016, 8: 30281–30286
45 Wang Z R, Rao M Y, Midya R, et al. Threshold switching of Ag or Cu in dielectrics: materials, mechanism, and applications. Adv Funct Mater, 2018, 28: 1704862
46 Zhu Y X, Shin B, Liu G X, et al. Electrospun ZnSnO nanofibers for neuromorphic transistors with ultralow energy consumption. IEEE Electron Device Lett, 2019, 40: 1776–1779
47 Zhang C, Wang S Y, Zhao X L, et al. Sub-femtojoule-energy-consumption conformable synaptic transistors based on organic single-crystalline nanoribbons. Adv Funct Mater, 2020, 31: 2007894
48 Liu L, Cui B, Xu W, et al. Highly aligned indium zinc oxide nanowire-based artificial synapses with low-energy consumption. J Industrial Eng Chem, 2020, 88: 111–116
49 Zhu Y X, Peng B C, Zhu L, et al. IGZO nanofiber photoelectric neuromorphic transistors with indium ratio tuned synaptic plasticity. Appl Phys Lett, 2022, 121: 133502
50 Wang J, Yang B, Dai S L, et al. Weak light-stimulated synaptic transistors based on $MoS_2$/organic semiconductor heterojunction for neuromorphic computing. Adv Mater Technol, 2023, 8: 2300449